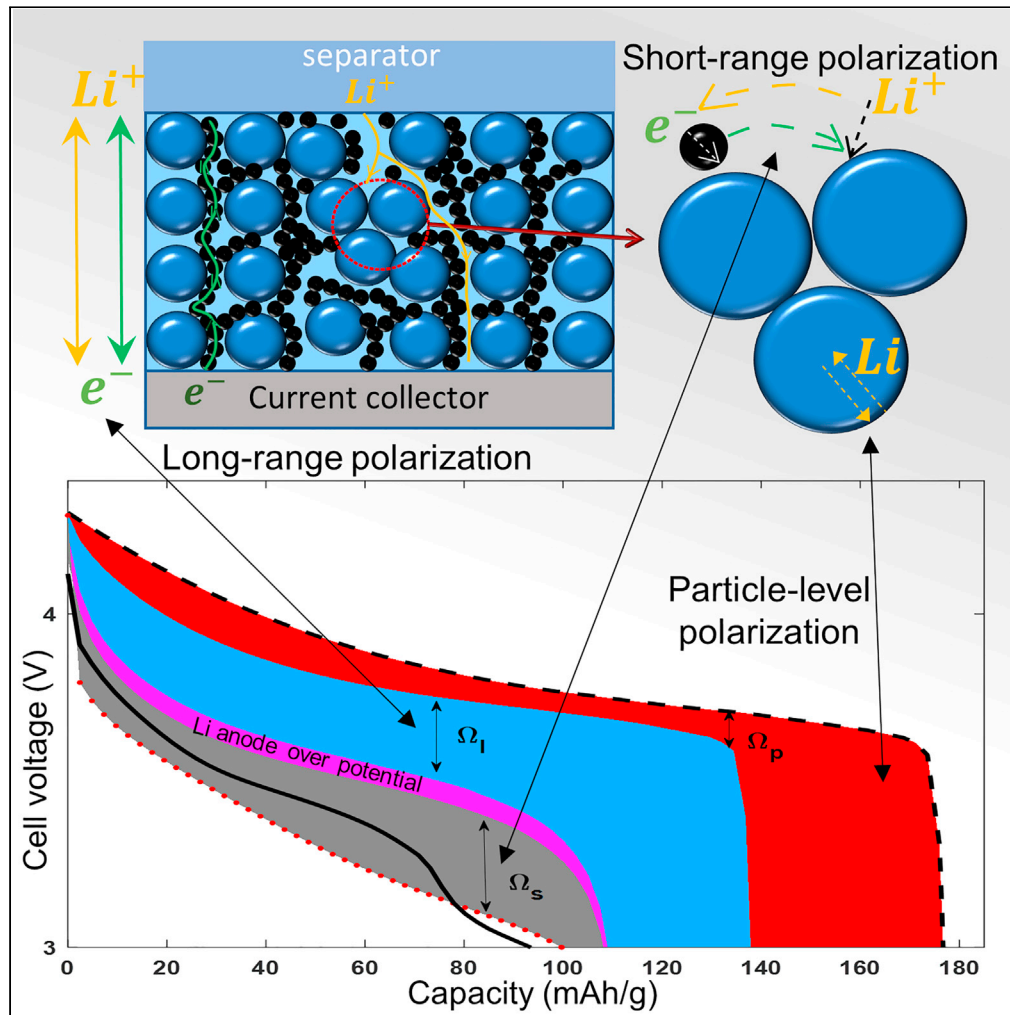


## Article

## A limitation map of performance for porous electrodes in lithium-ion batteries



Hamid Hamed,  
Lowie Henderick,  
Behnam Ghalami  
Choobar, Jan  
D'Haen,  
Christophe  
Detavernier, An  
Hardy,  
Mohammadhossein  
Safari

momo.safari@uhasselt.be

**Highlights**

Comprehensive map of performance limitations for  $\text{LiNi}_x\text{Mn}_y\text{Co}_{1-x-y}\text{O}_2$  electrodes

Development of a methodology to study the polarization in a lithium-ion battery

Revealing the limiting factors to the performance of  $\text{LiNi}_x\text{Mn}_y\text{Co}_{1-x-y}\text{O}_2$  electrodes

Model validation with orthogonal experimentation

Hamed et al., iScience 24, 103496  
December 17, 2021 © 2021  
The Author(s).  
<https://doi.org/10.1016/j.isci.2021.103496>



## Article

# A limitation map of performance for porous electrodes in lithium-ion batteries

Hamid Hamed,<sup>1,2</sup> Lowie Henderick,<sup>3</sup> Behnam Ghalami Choobar,<sup>1</sup> Jan D'Haen,<sup>1,4</sup> Christophe Detavernier,<sup>3</sup> An Hardy,<sup>1,2,4</sup> and Mohammadhossein Safari<sup>1,2,4,5,\*</sup>

## SUMMARY

**Driven by expanding interest in battery storage solutions and the success story of lithium-ion batteries, the research for the discovery and optimization of new battery materials and concepts is at peak. The generation of experimental (dis)charge data using coin cells is fast and feasible and proves to be a favorite practice in the battery research labs. The quantitative interpretation of the data, however, is not trivial and decelerates the process of screening and optimization of electrode materials and recipes. Here, we introduce the concept of polarographic map and demonstrate how it can be leveraged to quantify the contribution of different non-equilibrium phenomena to the performance limitation and total polarization of a lithium-ion cell. We showcase the accuracy and diagnostic power of this approach by preparing and analyzing the electrochemical performance of 54 sets of  $\text{LiNi}_x\text{Mn}_y\text{Co}_{1-x-y}\text{O}_2$  electrodes with different formulations and designs discharged in a range of 0.2C–5C.**

## INTRODUCTION

Innovation in battery technologies is one of the important elements in the global effort to combat climate change. A sustainable worldwide transition in the transport sector to electric vehicles relies very much on further decline in the price and increase in the safety and energy density of lithium-ion batteries (Gray and Hall, 2020). This inspires the ongoing research for the discovery of new materials, in particular by pushing the boundaries of insertion capacity in the active-material particles like  $\text{LiNi}_x\text{Mn}_y\text{Co}_{1-x-y}\text{O}_2$  (NMC) (Arico et al., 2011; Chen et al., 2010; Ji et al., 2020; Kang and Ceder, 2009; Manthiram, 2020; Nitta et al., 2015; Zhang et al., 2021b) and porous electrode formulations (Evanoff et al., 2012; Huang et al., 2019; Zhang et al., 2021a) with high energy and power densities.

Coin cells are very widely in use in the research community to evaluate the collective impact of the new materials or electrode designs on the performance of a lithium-ion cell composed of two facing electrodes and an electrolyte/separator in between (Chen et al., 2019; Murray et al., 2019). The interpretation of the voltage-current signals from such an all-embracing yet feasible characterization approach, however, is not intuitive if one aims to decipher between the differential contributions from each individual component when some modifications are introduced to the baseline materials and cell design parameters (Besnard et al., 2017; Doyle and Newman, 1997; Jiang and Peng, 2016). This is mainly because of the non-linear aggregate effects in determining the deviation of the instantaneous voltage ( $V$ ) from the equilibrium voltage ( $V_{eq}$ ), namely polarization ( $\eta = V - V_{eq}$ ) of an electrochemical system composed of porous electrodes rather than planar electrodes (Fuller et al., 1994; Lu et al., 2020a, 2020b).

The electrochemical behavior of the porous electrode is a collective outcome of individual responses from its many active-material particles distributed over the 3D space of the electrode (Figures 1A–1D). Therefore, while draining cell capacity ( $\delta q$ ), the energy loss ( $\delta q\eta$ ) associated with the transport of electrons and lithium ions across the thickness of the electrode (Ebner et al., 2014; Oriksa et al., 2016) (long-range,  $\Omega_l$ ) adds up with that pertaining to the active-material particles (Lin et al., 2018; Tsai et al., 2018; Zheng et al., 2015) such as solid-state diffusion and charge transfer kinetics (particle level,  $\Omega_p$ ) and the short-range losses into the bargain ( $\Omega_s$ ), i.e.  $\delta q\eta = \Omega_p + \Omega_s + \Omega_l$ . The latter depends on the quality of the local contacts between the electronic and ionic percolation networks and the active-material particles (Hamed et al., 2020; Jiang et al., 2020; Morelly et al., 2018). The exact composition of the total polarization from the aforementioned three polarization subsets,  $\gamma_i = \frac{\Omega_i}{\Omega_p + \Omega_s + \Omega_l}$ ,  $i = p, s, l$ , depends not only on the intrinsic properties of the

<sup>1</sup>Institute for Materials Research (IMO-imomec), UHasselt, Martelarenlaan 42, B-3500 Hasselt, Belgium

<sup>2</sup>Energyville, Thor Park 8320, B-3600 Genk, Belgium

<sup>3</sup>Department of Solid State Sciences, Ghent University, Krijgslaan 281 S1, 9000 Gent, Belgium

<sup>4</sup>IMEC Division IMOMEC, BE-3590 Belgium

<sup>5</sup>Lead contact

\*Correspondence:  
[momo.safari@uhasselt.be](mailto:momo.safari@uhasselt.be)  
<https://doi.org/10.1016/j.isci.2021.103496>



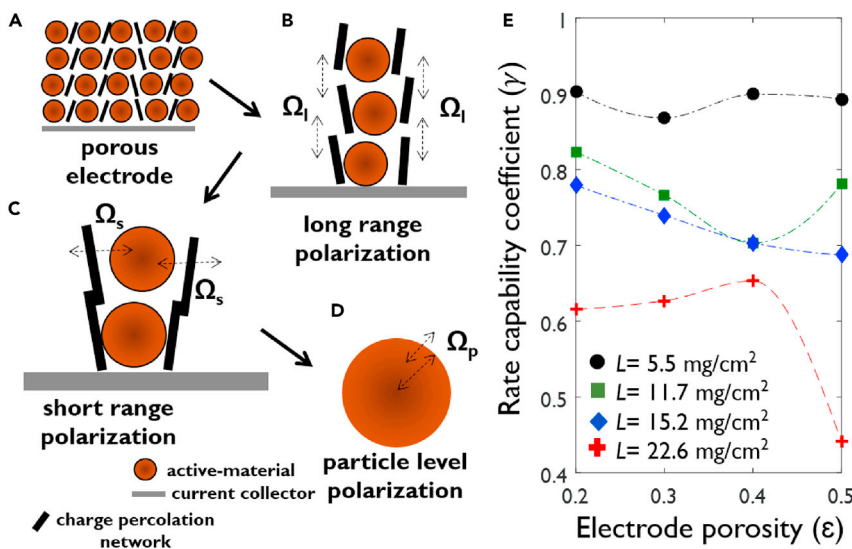


**Figure 1. Polarization categories and rate-capability of a porous electrode**

(A) a schematic representation of a porous electrode and the three major polarization subcategories limiting its rate-performance: (B) long range, (C) short range, (D) particle level.

(E) The rate capability coefficient of NMC622 electrodes from the reference batch as a function of electrode porosity,  $\epsilon = 0.2$  to 0.5, and active-material loading,  $L = 5.5$  to  $22.6 \text{ mg/cm}^2$ . It is important to note that the dashed lines are just for a visual guide.

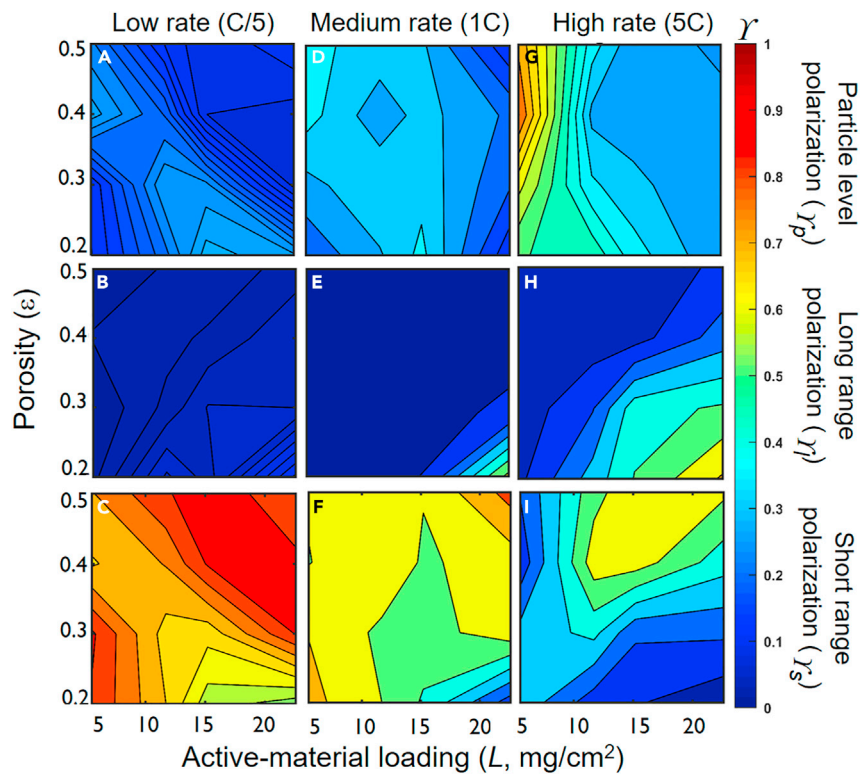
materials but also on the electrode recipe, preparation steps, and (dis)charge current (Besnard et al., 2017; Du et al., 2010; Nyman et al., 2010; Tian et al., 2019).

Here, we introduce the concept of polarographic map for a porous electrode to facilitate the design and optimization of new materials for lithium-ion cells. This map illustrates the composition of polarization in a porous electrode from three subsets of particle level, short-range, and long-range and their sensitivity to the active-material loading ( $\text{mg}/\text{cm}^2$ ), porosity (degree of calendering), and C-rate. This could serve as a diagnostic tool to identify the performance bottlenecks and to guide devising efficient strategies of improvement and material screening. The concept is showcased for the NMC family of active materials.

## RESULTS AND DISCUSSIONS

We first construct a map based on a comprehensive polarization analysis of a base batch including 16 Li-Ni<sub>0.6</sub>Mn<sub>0.2</sub>Co<sub>0.2</sub>O<sub>2</sub> (NMC622) electrodes of same active-mass content ( $f_a = 0.92$ ), but of different active-material loading ( $L = 5$  to  $23 \text{ mg}/\text{cm}^2$ ) and porosity ( $\epsilon = 0.2$  to 0.5). Next, the performance of 48 new electrode variants of the base batch is presented and discussed in the perspective of the added value in using the polarographic maps in battery research. The new cell variants were prepared by inducing three types of modifications in the original cell, namely by using either NMC particles with a different intrinsic solid-state diffusion coefficient (NMC111), or NMC622 particles ALD-coated with a layer of TiO<sub>2</sub>, or by using a thicker separator.

A rate-capability coefficient ( $0 \leq \gamma \leq 1$ ) was obtained for every Li/NMC cell by analyzing the galvanostatic (dis)charge over a broad range of C-rates (0.2C–5C). This coefficient reflects the relative retention of discharge energy delivered by the cell upon every doubling in the discharge current (see STAR Methods). The rate capability coefficient of the 16 reference NMC electrodes are scattered in Figure 1E as a function of NMC loading and electrode porosity. We observe a clear inverse correlation between  $\gamma$  and the active-material loading,  $\left.\frac{\partial \gamma}{\partial L}\right|_{\epsilon} \leq 0$ , which is in line with the commonly observed power fade at high electrode loadings (Heubner et al., 2019; Zhao et al., 2015). The effect of porosity ( $\epsilon$ ), however, on the rate performance of the electrode is less intuitive to be generalized and depends on the electrode loading. The sensitivity of rate-performance to the electrode porosity at a given loading  $\left(\left.\frac{\partial \gamma}{\partial \epsilon}\right|_L\right)$  begins to intensify for loadings

**Figure 2. Polarographic map for NMC electrode**

Polarographic map for the NMC electrode visualizing the contributions to the total electrode polarization from the irreversible phenomena originating from the three distinctive subcategories: particle level, long range, short range. The composition of the electrode polarization is displayed with the contour maps as a function of electrode porosity and active material loading and for three levels of discharge rates: low rate (C/5), medium rate (1C), and high rate (5C). The color bar codes the polarization contributions ( $0 \leq \gamma_i \leq 1$ ) between the dark blue and dark red. It is important to note that each subplot consist of 16 data points and the rest of the image is linearly colored just as a visual guidance.

above  $5 \text{ mg}/\text{cm}^2$  and is non-monotonic. For instance, at  $L = 22.6 \text{ mg}/\text{cm}^2$ , the initial decrease in porosity from 0.5 to 0.4 is beneficial to the rate performance of the electrode  $\left(\frac{\partial \gamma}{\partial \epsilon}\right|_{L=23} < 0$ , whereas further decrease in porosity ( $0.2 < \epsilon < 0.4$ ) lowers the power rating of the electrode  $\left(\frac{\partial \gamma}{\partial \epsilon}\right|_{L=23} > 0$ .

This observation highlights the complicated superposition of the ionic and electronic transport limitations over the short and long ranges in determining the rate performance of a porous electrode. Calendering the electrode will bring the active-material particles, carbon, and binder into a closer contact and therefore promotes the short- and long-range electronic conduction through the electrode thickness. On the other hand, a lower porosity can be detrimental to the rate of charge transport in the electrolyte phase and charge-transfer kinetics on account of higher tortuosity and lower specific surface area between the active-material particles and electrolyte, respectively. Further quantitative insights can only be obtained by splitting the total cell polarization among the involved sub-phenomena by comparing the experimental data against a comprehensive model (Malifarge et al., 2018).

To conduct a detailed polarization analysis we used a macroscopic physics-based model (see [supplemental information](#)) to simulate the experimental rate performance data of the 16 NMC622 electrodes from the reference batch at three constant-current loads equivalent to C/5, 1C, and 5C. The constructed polarization map is presented in [Figure 2](#). The polarization at lower C-rates is dominantly induced by the poor electronic and ionic contacts between the active-material particles and the percolation networks irrespective of the electrode loading and porosity ( $\gamma_s > 0.4$ ). This is in line with the general expectation that the power limitation of a porous electrode at sufficiently low C-rates becomes less sensitive to the

electrode thickness and the transport limitations in the bulk of electrode and electrolyte phases (Malifarge et al., 2018).

Noteworthy is the significance of short-range polarization ( $\gamma_s > 0.7$ ) for electrodes with low porosity and low loading as well as those with high porosity and high loading (Figure 2C). At higher C-rates the performance limitation of the cell is very sensitive to the loading and porosity of the electrode. In other words, the power limitation induced by the sluggish electronic conduction between the current collector and the separator is more pronounced at thicker electrodes. Similarly, the ionic conduction in the electrolyte bulk is associated with higher polarization when decreasing the electrode porosity in thicker electrodes. The particle level polarization has a considerable impact ( $\gamma_p > 0.5$ ) on the rate performance at low active-material loading regardless of the electrode porosity (Figure 2G). The rate performance for loadings above  $10 \text{ mg/cm}^2$  and porosity below 0.4 is mainly controlled by the long-range ionic transport limitations (Figure 2H). Electrodes with higher loading and higher porosity values, however, are more influenced by the short-range electronic limitations at high C-rates (Figure 2I).

The polarographic map facilitates the identification of the rate determining phenomena as a function of the electrode recipe. Therefore, the improvement strategies can be accordingly concentrated on the most blameworthy aspect of the electrode components. For instance, a significant share of short-range polarization which was revealed for the electrodes considered in this study (Figures 2C, 2F, and 2I) highlights the relatively low intrinsic conductivity of the NMC particles which could be improved by a strategy such as particle coating with a conductive layer (Yu et al., 2019; Kalluri et al., 2017; Wang et al., 2015). We showcased such an approach by covering the NMC particles with a thin  $\text{TiO}_2$  layer, known as a good conductor (Chen et al., 2014; Gao et al., 2018b; Wu et al., 2009), with the aid of atomic-layer deposition (see supplemental information) (Chen et al., 2010; Meng et al., 2012). The ALD-coated particles were used to make 16 new electrodes of similar formulation to the original batch and analyzed for the electrochemical performance. As expected, a substantial boost to the rate performance is gained for the  $\text{TiO}_2$ -coated samples relative to that of the bare ones (Figure S6). Moreover, the  $\text{TiO}_2$  layer induces a clear change in the sign of  $\left.\frac{\partial y}{\partial t}\right|_e$  highlighting the efficacy of this treatment in decreasing the short-range electronic contact resistance between the NMC particles and the surrounding carbon network (Figure S6).

The validity of the formulation-polarization correspondence provided by the polarographic map was put to the extra tests by considering another two new design variants of the NMC electrodes. The second group of tests were conducted on the cells assembled with the original sixteen NMC622 electrodes but with two separators in order to manipulate the long-range transport limitations inside the electrolyte with respect to the reference design. In the third group, 16 NMC111 electrodes with analogous formulation to the base batch were prepared to examine the sensitivity of the polarographic map in response to the design modifications at particle level. A significant intra-particle sensitivity is expected in view of the clear difference between the solid-state lithium diffusion in NMC111 and NMC622 particles (Noh et al., 2013). The relative change in the discharge energy ( $\Delta E$ ) of the three new design groups of electrodes compared to the reference batch is summarized Figure 3.

In each group (sub-figures in row), the 48  $\Delta E$  data points, corresponding to the sixteen different electrodes' formulations discharged at three C-rates, are scattered against 3 different types of horizontal coordinates. These coordinates are  $\gamma_p$ ,  $\gamma_l$ , and  $\gamma_s$  and pair the  $\Delta E$  data each time with one of the polarization indicators corresponding to the respective electrode formulation and C-rate (read from polarographic map, Figure 2). A strong positive correlation (Table S5) between the relative change in the electrode performance ( $\Delta E$ ) and  $\gamma_p$ ,  $\gamma_l$ , and  $\gamma_s$  is observed only for the diagonal sub-Figures 3C, 3E, and 3G, respectively, which demonstrates that the polarographic map is properly zoned and has a high sensitivity to the variations in design parameters.

Although the concept of polarographic map was developed and demonstrated for the NMC electrodes it is not limited to the lithium-ion batteries. Once a reliable physics-based model of the battery is available, the methodology developed in this work can be followed to obtain a detailed polarization map for other battery chemistries. Such maps are expected to be very helpful in the further development and optimization of

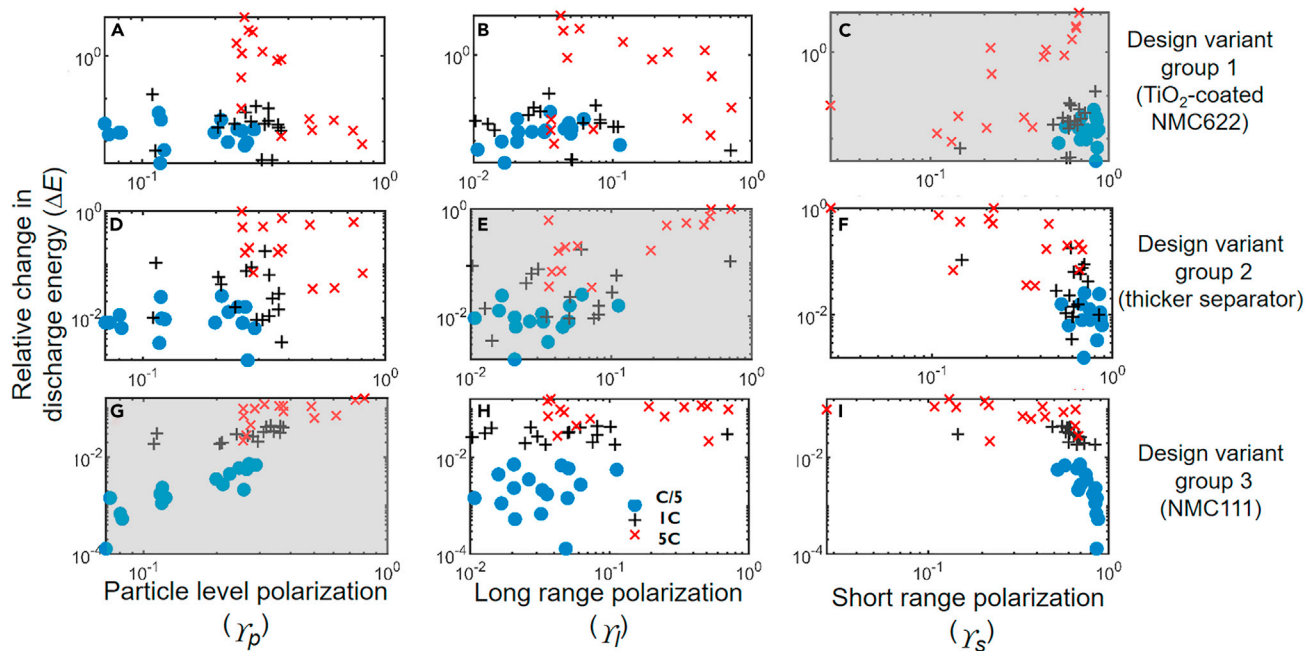


**Figure 3. Variants of electrode design in the perspective of polarographic map**

The fractional change in the discharge energy ( $\Delta E$ ) of Li|NMC cells with  $\text{TiO}_2$ -coated NMC622 and thick separator, and NMC111, relative to the reference Li|NMC622 cell.  $\Delta E$  Data are scattered against three different coordinates representing the fractional contribution from particle level ( $\gamma_p$ ), long-range transport ( $\gamma_l$ ), and short-range transport ( $\gamma_s$ ) in the cell polarization.

solid-state batteries where the intimate contact between the active-material particles and the solid electrolyte, i.e., short-range polarization is believed to be an important limiting factor to the performance. Similarly, the design of porous electrodes for conversion chemistries such as sulfur can be facilitated with the help of the methodology presented in this work. There are, however, more complexities expected in setting up a reliable modeling framework that accounts for the peculiarities of the conversion reaction mechanisms. For instance, in lithium-sulfur batteries, the role of the solution-mediated charge transfer mechanisms such as disproportionation reactions in the electrolyte bulk needs to be properly integrated in the model structure.

## CONCLUSIONS

In this work, we introduced the concept of polarographic map as a powerful tool in the design and evaluation of porous electrodes for lithium-ion battery applications. This map illustrates the relative significance of different sources of polarization in a porous electrode as a function of formulation and discharge load. The overall polarization is decomposed into the contributions from three groups of irreversible processes relevant to the active-material particles such as solid-state diffusion and those related to the charge transport over the short and long ranges in the electrode. The concept was showcased for the NMC-based electrodes by drawing up a polarographic map after a thorough analysis of the discharge performance for sixteen porous electrodes of different formulations at C/5, 1C, and 5C. The accuracy and diagnostic power of the map were demonstrated with the help of performance data from 48 new electrodes with different designs. This map proves to be very efficient in the identification of the performance bottlenecks in lithium-ion cells and can be employed to facilitate the rational design and optimization of the cell and electrode components.

## Limitations of the study

Care should be taken in the direct generalization of the polarization trends of the NMC electrode to other electrodes used in lithium-ion batteries. For instance, the relative significance of particle-level, short-range, and long-range polarization can be significantly different in the electrodes made up of active-material particles with very different particle-size distribution and intrinsic conductivity.

#### List of symbols

|                        |  |
|------------------------|--|
| $a_k$                  | active surface area of kth particle group per unit volume of electrode,                              |
| $c_s$                  | Solid-state Li concentration inside active material particle,  |
| $c_{LiPF_6}$           | Salt concentration in the electrolyte,   |
| $c_{max}$              | Maximum concentration of Li in active material particle,   |
| $D_{l,m}^{eff}$        | Effective ionic diffusion of electrolyte at the domain 'm'; i.e. cathode or separator,               |
| $D_s$                  | Solid-state diffusion coefficient,   |
| $I$                    | Total current density referred to the separator area,  |
| $i_1$                  | Current density inside the solid matrix,   |
| $i_2$                  | Current density inside the electrolyte,  |
| $i_{n,k}$              | Interfacial current density of kth particle group referred to the active surface area of this group, |
| $i_f^0, i_f^0$         | Exchange current density for NMC and Li electrode,   |
| $F$                    | Faraday's constant, 96,487   |
| $k_{l,m}^{eff}$        | Effective ionic conductivity of electrolyte at the domain 'm'; i.e. cathode or separator,            |
| $k_c^0$                | Rate constant of electrochemical reaction at the cathode,  |
| $l_c$                  | Cathode thickness, m   |
| $l_{sep}$              | Separator thickness, m   |
| $R$                    | Universal gas constant, $8.3145 \frac{J}{mol \cdot K}$   |
| $R_k$                  | Inter-particle resistance of kth particle group  |
| $R_{p,k}$              | Radius of the kth particle group (m)   |
| $R$                    | Radial position inside solid particle  |
| $T$                    | Temperature, K   |
| $t_0^+$                | Cation transference number   |
| $U_k$                  | Open circuit potential for the kth particle group  |
| $x$                    | Linear position in cell or normalized Li concentration inside NMC particle, depending on context     |
| Greek                  |  |
| $\beta, \beta_f$       | Charge transfer coefficient for NMC and Li electrode   |
| $\varepsilon$          | Electrode bulk porosity  |
| $\eta_k$               | Surface over potential of kth particle group, V  |
| $\varphi_1, \varphi_2$ | Solid-phase and electrolyte potential, V   |
| $\rho_i$               | Density of component i,  |
| $\gamma$               | Rate capability coefficient  |

## STAR★METHODS

Detailed methods are provided in the online version of this paper and include the following:

- KEY RESOURCES TABLE
- RESOURCE AVAILABILITY
  - Lead contact
  - Material availability
  - Data and code availability
- METHOD DETAILS
  - Electrode preparation
  - Rate capability coefficient
  - Electrochemical tests
  - Particle size distribution (PSD)
  - ALD coating
  - Polarization analysis
  - Statistical analysis

## SUPPLEMENTAL INFORMATION

Supplemental information can be found online at <https://doi.org/10.1016/j.isci.2021.103496>.

## ACKNOWLEDGMENTS

The authors are grateful for financial support to FWO-Vlaanderen (SBO XL-Lion, S005017N). H. H. and M.S. acknowledge Prof. Wouter Marchal for the support in PSD measurements.

## AUTHOR CONTRIBUTIONS

M.S supervised the project. H.H and M.S designed the concept and methodology and wrote the paper together. All the experiments and investigations were performed by H.H except for the ALD coating experiments and corresponding characterizations that were performed by L.H and supervised by C.D. The SEM for porous electrodes was performed by J.D. The numerical simulations were performed by H.H and the optimization algorithms for parametrization were developed and applied by H.H and B.G.C. All the authors contributed to the discussions and interpretations of the results and editing and finalizing the manuscript.

## DECLARATION OF INTERESTS

The authors declare that there is no conflict of interest.

Received: August 24, 2021

Revised: November 1, 2021

Accepted: November 19, 2021

Published: December 17, 2021

## SUPPORTING CITATIONS

The following reference appears in the Supplemental information: Mao et al., 2015; Nyman et al., 2008.

## REFERENCES

- Amin, R., and Chiang, Y.-M. (2016). Characterization of electronic and ionic transport in Li<sub>1-x</sub>NiO<sub>x</sub>·33MnO<sub>x</sub>·33CoO<sub>x</sub>·33O<sub>2</sub> (NMC333) and Li<sub>1-x</sub>NiO<sub>x</sub>·50MnO<sub>x</sub>·20CoO<sub>x</sub>·30O<sub>2</sub> (NMC523) as a function of Li content. *J. Electrochem. Soc.* 163, A1512.
- Appiah, W.A., Park, J., Song, S., Byun, S., Ryou, M.-H., and Lee, Y.M. (2016). Design optimization of LiNiO<sub>x</sub>·6CoO<sub>x</sub>·2MnO<sub>x</sub>·2O<sub>2</sub>/graphite lithium-ion cells based on simulation and experimental data. *J. Power Sources* 319, 147–158.
- Arico, A.S., Bruce, P., Scrosati, B., Tarascon, J.-M., and van Schalkwijk, W. (2011). Nanostructured materials for advanced energy conversion and storage devices. *Nat. Mater.* 10, 148–159.
- Besnard, N., Etiemble, A., Douillard, T., Dubrunfaut, O., Tran-Van, P., Gautier, L., Franger, S., Badot, J.C., Maire, E., and Lestriez, B. (2017). Multiscale morphological and electrical characterization of charge transport limitations to the power performance of positive electrode blends for lithium-ion batteries. *Adv. Energy Mater.* 7, 1602239.
- Chen, S., Niu, C., Lee, H., Li, Q., Yu, L., Xu, W., Zhang, J.-G., Dufek, E.J., Whittingham, M.S., and Meng, S. (2019). Critical parameters for evaluating coin cells and pouch cells of rechargeable Li-metal batteries. *Joule* 3, 1094–1105.
- Chen, Y., Zhang, Y., Chen, B., Wang, Z., and Lu, C. (2014). An approach to application for LiNiO<sub>x</sub>·6CoO<sub>x</sub>·2MnO<sub>x</sub>·2O<sub>2</sub> cathode material at high cutoff voltage by TiO<sub>2</sub> coating. *J. Power Sources* 256, 20–27.
- Chen, Z., Qin, Y., Amine, K., and Sun, Y.-K. (2010). Role of surface coating on cathode materials for lithium-ion batteries. *J. Mater. Chem.* 20, 7606–7612.
- Chouchane, M., Primo, E.N., and Franco, A.A. (2020). Mesoscale effects in the extraction of the solid-state lithium diffusion coefficient values of battery active materials: physical insights from 3D modeling. *J. Phys. Chem.* 11, 2775–2780.
- Churikov, A., Ivanishchev, A., Ushakov, A., and Romanova, V. (2014). Diffusion aspects of lithium intercalation as applied to the development of electrode materials for lithium-ion batteries. *J. Solid State Electrochem.* 18, 1425–1441.
- Doyle, M., Fuller, T.F., and Newman, J. (1993). Modeling of galvanostatic charge and discharge of the lithium/polymer/insertion cell. *J. Electrochem. Soc.* 140, 1526.
- Doyle, M., and Newman, J. (1997). Analysis of capacity-rate data for lithium batteries using simplified models of the discharge process. *J. Appl. Electrochem.* 27, 846–856.
- Du, W., Gupta, A., Zhang, X., Sastry, A.M., and Shyy, W. (2010). Effect of cycling rate, particle size and transport properties on lithium-ion cathode performance. *Int. J. Heat Mass Transfer* 53, 3552–3561.
- Ebner, M., Chung, D.W., García, R.E., and Wood, V. (2014). Tortuosity anisotropy in lithium-ion battery electrodes. *Adv. Energy Mater.* 4, 1301278.
- Evanoff, K., Khan, J., Balandin, A.A., Magasinski, A., Ready, W.J., Fuller, T.F., and Yushin, G. (2012). Towards ultrathick battery electrodes: aligned carbon nanotube-enabled architecture. *Adv. Mater.* 24, 533–537.
- Fuller, T.F., Doyle, M., and Newman, J. (1994). Simulation and optimization of the dual lithium ion insertion cell. *J. Electrochem. Soc.* 141, 1.
- Gallagher, K.G., Trask, S.E., Bauer, C., Woehrle, T., Lux, S.F., Tschech, M., Lamp, P., Polzin, B.J., Ha, S., and Long, B. (2015). Optimizing areal capacities through understanding the limitations of lithium-ion electrodes. *J. Electrochem. Soc.* 163, A138.
- Gao, H., Wu, Q., Hu, Y., Zheng, J.P., Amine, K., and Chen, Z. (2018a). Revealing the rate-limiting Li-ion diffusion pathway in ultrathick electrodes for Li-ion batteries. *J. Phys. Chem.* 9, 5100–5104.
- Gao, H., Zeng, X., Hu, Y., Tileli, V., Li, L., Ren, Y., Meng, X., Maglia, F., Lamp, P., and Kim, S.-J. (2018b). Modifying the surface of a high-voltage lithium-ion cathode. *ACS Appl. Energy Mater.* 1, 2254–2260.
- Grey, C.P., and Hall, D.S. (2020). Prospects for lithium-ion batteries and beyond—a 2030 vision. *Nat. Commun.* 11, 1–4.
- Hamed, H., Yari, S., D'Haen, J., Renner, F.U., Reddy, N., Hardy, A., and Safari, M. (2020). Demystifying charge transport limitations in the porous electrodes of lithium-ion batteries. *Adv. Energy Mater.* 10, 2002492.
- Heubner, C., Nickol, A., Seeba, J., Reuber, S., Junker, N., Wolter, M., Schneider, M., and Michaelis, A. (2019). Understanding thickness and porosity effects on the electrochemical performance of LiNiO<sub>x</sub>·6CoO<sub>x</sub>·2MnO<sub>x</sub>·2O<sub>2</sub>-based cathodes for high energy Li-ion batteries. *J. Power Sources* 419, 119–126.
- Huang, C., Dontigny, M., Zaghib, K., and Grant, P.S. (2019). Low-tortuosity and graded lithium ion battery cathodes by ice templating. *J. Mater. Chem. A* 7, 21421–21431.
- Butzenlaub, T., Asthana, A., Becker, J., Wheeler, D., Zengerle, R., and Thiele, S. (2013). FIB/SEM-based calculation of tortuosity in a porous LiCoO<sub>2</sub> cathode for a Li-ion battery. *Electrochem. Commun.* 27, 77–80.
- Ji, H., Wu, J., Cai, Z., Liu, J., Kwon, D.-H., Kim, H., Urban, A., Papp, J.K., Foley, E., and Tian, Y. (2020). Ultrahigh power and energy density in partially ordered lithium-ion cathode materials. *Nat. Energy* 5, 213–221.
- Jiang, F., and Peng, P. (2016). Elucidating the performance limitations of lithium-ion batteries

due to species and charge transport through five characteristic parameters. *Sci. Rep.* 6, 1–18.

Jiang, Z., Li, J., Yang, Y., Mu, L., Wei, C., Yu, X., Pianetta, P., Zhao, K., Cloetens, P., and Lin, F. (2020). Machine-learning-revealed statistics of the particle-carbon/binder detachment in lithium-ion battery cathodes. *Nat. Commun.* 11, 1–9.

Kalluri, S., Yoon, M., Jo, M., Park, S., Myeong, S., Kim, J., Dou, S.X., Guo, Z., and Cho, J. (2017). Surface engineering strategies of layered LiCoO<sub>2</sub> cathode material to realize high-energy and high-voltage Li-ion cells. *Adv. Energy Mater.* 7, 1601507.

Kang, B., and Ceder, G. (2009). Battery materials for ultrafast charging and discharging. *Nature* 458, 190–193.

Kehrwald, D., Shearing, P.R., Brandon, N.P., Sinha, P.K., and Harris, S.J. (2011). Local tortuosity inhomogeneities in a lithium battery composite electrode. *J. Electrochem. Soc.* 158, A1393.

Landesfeind, J., Eldiven, A., and Gasteiger, H.A. (2018). Influence of the binder on lithium ion battery electrode tortuosity and performance. *J. Electrochem. Soc.* 165, A1122.

Lin, Q., Guan, W., Meng, J., Huang, W., Wei, X., Zeng, Y., Li, J., and Zhang, Z. (2018). A new insight into continuous performance decay mechanism of Ni-rich layered oxide cathode for high energy lithium ion batteries. *Nano Energy* 54, 313–321.

Longrie, D., Deduytsche, D., and Detavernier, C. (2014). Reactor concepts for atomic layer deposition on agitated particles: a review. *J. Vac. Sci. Technol. A* 32, 010802.

Longrie, D., Deduytsche, D., Haemers, J., Driesen, K., and Detavernier, C. (2012). A rotary reactor for thermal and plasma-enhanced atomic layer deposition on powders and small objects. *Surf. Coat. Technol.* 213, 183–191.

Lu, X., Bertei, A., Finegan, D.P., Tan, C., Daemi, S.R., Weaving, J.S., O'Regan, K.B., Heenan, T.M., Hinds, G., and Kendrick, E. (2020a). 3D microstructure design of lithium-ion battery electrodes assisted by X-ray nano-computed tomography and modelling. *Nat. Commun.* 11, 1–13.

Lu, X., Daemi, S.R., Bertei, A., Kok, M.D., O'Regan, K.B., Rasha, L., Park, J., Hinds, G., Kendrick, E., and Brett, D.J. (2020b). Microstructural evolution of battery electrodes during calendering. *Joule* 4, 2746–2768.

Malifarge, S., Delobel, B., and Delacourt, C. (2017). Determination of tortuosity using impedance spectra analysis of symmetric cell. *J. Electrochim. Soc.* 164, E3329.

Malifarge, S., Delobel, B., and Delacourt, C. (2018). Experimental and modeling analysis of graphite electrodes with various thicknesses and porosities for high-energy-density Li-ion batteries. *J. Electrochim. Soc.* 165, A1275.

Manthiram, A. (2020). A reflection on lithium-ion battery cathode chemistry. *Nat. Commun.* 11, 1–9.

Mao, Z., Farkhondeh, M., Pritzker, M., Fowler, M., and Chen, Z. (2015). Multi-particle model for a commercial blended lithium-ion electrode. *J. Electrochim. Soc.* 163, A458.

Mattelaer, F., Vereecken, P.M., Dendooven, J., and Detavernier, C. (2017). The influence of ultrathin amorphous ALD alumina and Titania on the rate capability of anatase TiO<sub>2</sub> and LiMn<sub>2</sub>O<sub>4</sub> Lithium ion battery electrodes. *Adv. Mater. Inter.* 4, 1601237.

Meng, X., Yang, X.Q., and Sun, X. (2012). Emerging applications of atomic layer deposition for lithium-ion battery studies. *Adv. Mater.* 24, 3589–3615.

Morelly, S.L., Alvarez, N.J., and Tang, M.H. (2018). Short-range contacts govern the performance of industry-relevant battery cathodes. *J. Power Sources* 387, 49–56.

Murray, V., Hall, D.S., and Dahn, J. (2019). A guide to full coin cell making for academic researchers. *J. Electrochim. Soc.* 166, A329.

Nitta, N., Wu, F., Lee, J.T., and Yushin, G. (2015). Li-ion battery materials: present and future. *Mater. Today* 18, 252–264.

Noh, H.-J., Youn, S., Yoon, C.S., and Sun, Y.-K. (2013). Comparison of the structural and electrochemical properties of layered Li[NixCoyMnz]O<sub>2</sub> (x=1/3, 0.5, 0.6, 0.7, 0.8 and 0.85) cathode material for lithium-ion batteries. *J. Power Sources* 233, 121–130.

Nyman, A., Behm, M., and Lindbergh, G. (2008). Electrochemical characterisation and modelling of the mass transport phenomena in LiPF<sub>6</sub>-EC-EMC electrolyte. *Electrochim. Acta* 53, 6356–6365.

Nyman, A., Zavalis, T.G., Elger, R., Behm, M., and Lindbergh, G. (2010). Analysis of the polarization in a Li-ion battery cell by numerical simulations. *J. Electrochim. Soc.* 157, A1236.

Orikasa, Y., Gogyo, Y., Yamashige, H., Katayama, M., Chen, K., Mori, T., Yamamoto, K., Masese, T., Inada, Y., and Ohta, T. (2016). Ionic conduction in lithium ion battery composite electrode governs cross-sectional reaction distribution. *Sci. Rep.* 6, 1–6.

Pouraghajian, F., Knight, H., Wray, M., Mazzeo, B., Subbaraman, R., Christensen, J., and Wheeler, D. (2018). Quantifying tortuosity of porous Li-ion battery electrodes: comparing polarization-interrupt and blocking-electrolyte methods. *J. Electrochim. Soc.* 165, A2644.

Thorat, I.V., Stephenson, D.E., Zacharias, N.A., Zaghib, K., Harb, J.N., and Wheeler, D.R. (2009). Quantifying tortuosity in porous Li-ion battery materials. *J. Power Sources* 188, 592–600.

Tian, R., Park, S.-H., King, P.J., Cunningham, G., Coelho, J., Nicolosi, V., and Coleman, J.N. (2019). Quantifying the factors limiting rate performance in battery electrodes. *Nat. Commun.* 10, 1–11.

Tsai, P.-C., Wen, B., Wolfman, M., Choe, M.-J., Pan, M.S., Su, L., Thornton, K., Cabana, J., and Chiang, Y.-M. (2018). Single-particle

measurements of electrochemical kinetics in NMC and NCA cathodes for Li-ion batteries. *Energy Environ. Sci.* 11, 860–871.

Usseglio-Viretta, F.L., Colclasure, A., Mistry, A.N., Claver, K.P.Y., Pouraghajian, F., Finegan, D.P., Heenan, T.M., Abraham, D., Mukherjee, P.P., and Wheeler, D. (2018). Resolving the discrepancy in tortuosity factor estimation for Li-ion battery electrodes through micro-macro modeling and experiment. *J. Electrochim. Soc.* 165, A3403.

Wang, K.X., Li, X.H., and Chen, J.S. (2015). Surface and interface engineering of electrode materials for lithium-ion batteries. *Adv. Mater.* 27, 527–545.

Wu, F., Wang, M., su, Y., Chen, S., and Xu, B. (2009). Effect of TiO<sub>2</sub>-coating on the electrochemical performances of LiCo<sub>1/3</sub>Ni<sub>1/3</sub>Mn<sub>1/3</sub>O<sub>2</sub>. *J. Power Sources* 191, 628–632.

Yari, S., Hamed, H., D'haen, J., van Bael, M.K., Renner, F.U., Hardy, A., and Safari, M. (2020). Constructive versus destructive heterogeneity in porous electrodes of lithium-ion batteries. *ACS Appl. Energy Mater.* 3, 11820–11829.

Yu, F.-D., Que, L.-F., Xu, C.-Y., Wang, M.-J., Sun, G., Duh, J.-G., and Wang, Z.-B. (2019). Dual conductive surface engineering of Li-Rich oxides cathode for superior high-energy-density Li-Ion batteries. *Nano Energy* 59, 527–536.

Zahn, R., Lagadec, M.F., and Wood, V. (2017). Transport in lithium ion batteries: reconciling impedance and structural analysis. *ACS Energy Lett.* 2, 2452–2453.

Zhang, X., Hui, Z., King, S., Wang, L., Ju, Z., Wu, J., Takeuchi, K.J., Marschilok, A.C., West, A.C., and Takeuchi, E.S. (2021a). Tunable porous electrode architectures for enhanced Li-ion storage kinetics in thick electrodes. *Nano Lett.* 21, 5896–5904.

Zhang, X., Ju, Z., Zhu, Y., Takeuchi, K.J., Takeuchi, E.S., Marschilok, A.C., and Yu, G. (2021b). Multiscale understanding and architecture design of high energy/power lithium-ion battery electrodes. *Adv. Energy Mater.* 11, 2000808.

Zhao, R., Liu, J., and gu, J. (2015). The effects of electrode thickness on the electrochemical and thermal characteristics of lithium ion battery. *Appl. Energy* 139, 220–229.

Zheng, H., Li, J., Song, X., Liu, G., and Battaglia, V.S. (2012a). A comprehensive understanding of electrode thickness effects on the electrochemical performances of Li-ion battery cathodes. *Electrochim. Acta* 71, 258–265.

Zheng, H., Tan, L., Liu, G., Song, X., and Battaglia, V.S. (2012b). Calendering effects on the physical and electrochemical properties of Li[Ni<sub>1/3</sub>Mn<sub>1/3</sub>Co<sub>1/3</sub>]O<sub>2</sub> cathode. *J. Power Sources* 208, 52–57.

Zheng, J., Xu, P., Gu, M., Xiao, J., Browning, N.D., Yan, P., Wang, C., and Zhang, J.-G. (2015). Structural and chemical evolution of Li-and Mn-rich layered cathode material. *Chem. Mater.* 27, 1381–1390.

## STAR★METHODS

## KEY RESOURCES TABLE

| REAGENT or RESOURCE                           | SOURCE            | IDENTIFIER     |
|---|-------------------|----------------|
| Chemicals, peptides, and recombinant proteins |                   |                |
| Carbon black                                  | IMERYS- Super C45 | CAS:1333-86-4  |
| Polyvinylidene-fluoride                       | SOLEF 5130-SOLVAY | CAS:24937-79-9 |
| N-methyl pyrrolidine                          | Carl Roth GmbH    | CAS:872-50-4   |

## RESOURCE AVAILABILITY

## Lead contact

Further information should be directed to and will be fulfilled by the lead contact, Mohammadhosein Safari ([momo.safari@uhasselt.be](mailto:momo.safari@uhasselt.be)).

## Material availability

This study did not generate new material.

## Data and code availability

- The necessary data to analyze the results of this study has been documented in the main and supplemental documents.
- The governing equations needed to generate the code for physics-based model have been outlined in [Table S3](#).
- All additional information required to reproduce the results reported in this paper is available from the lead contact upon reasonable request.

## METHOD DETAILS

## Electrode preparation

$\text{LiNi}_{0.6}\text{Mn}_{0.2}\text{Co}_{0.2}\text{O}_2$  (commercial product), Carbon black (IMERYS Super C45), and polyvinylidene-fluoride (PVDF, SOLEF 5130-SOLVAY) dispersed in N-methyl pyrrolidine (NMP, Carl Roth GmbH) were used to prepare slurries for the NMC electrodes. Active material, carbon and 6%w/w PVDF in NMP solution were mixed followed by a stepwise addition of extra NMP solvent to get a homogeneous slurry.

Electrode laminates were prepared by doctor-blade coating of the slurry on an aluminum foil (20  $\mu\text{m}$ ). After drying at 80°C for 10 h, the electrodes were punched into 15 mm disks and weighted by a Thermo Fisher scientific balance with 0.01 mg of precision. The electrode thickness was measured using a Mitutoyo digital micrometer with a precision of 0.1  $\mu\text{m}$ . The porosity of the electrode ( $\varepsilon$ ) was obtained according to

$$\varepsilon = 1 - \frac{m \cdot \sum_i f_i}{l \cdot A} \quad (\text{Equation 1})$$

where  $m$  is the weight of coating,  $A$  is the electrode surface area,  $l$  is the electrode thickness,  $f_i$  and  $\rho_i$  are the mass-fraction and density of the component  $i$ , respectively. The error associated with calculating the porosity ([Table S1](#)) depends on the uncertainties associated with the measurement of the electrode thickness, electrode mass and electrode's ingredients' mass fractions:

$$\left(\frac{\Delta \varepsilon}{\varepsilon}\right)^2 = \left(\sum \frac{\Delta f_i}{f_i}\right)^2 + \left(\frac{\Delta m}{m}\right)^2 + \left(\frac{\Delta l}{l}\right)^2 \quad (\text{Equation 2})$$

Where  $\Delta f_i$ ,  $\Delta m$  and  $\Delta l$  are the errors in the measurement of the electrode recipe, electrode mass and electrode thickness, respectively. The physico-structural properties of the 16 electrodes are presented in [Table S1](#).

### Rate capability coefficient

As introduced in our previous work ([Hamed et al., 2020](#)), we used an empirical formalism in analogy with the Peukert's law to quantify the sensitivity of the energy (Y) of the NMC electrodes to the discharge current:

$$Y_j = \beta I_j^{-\alpha} \quad (\text{Equation 3})$$

where  $Y_j$  is the discharge energy at the C-rate  $I_j$ .  $\alpha > 0$  and  $\beta > 0$  are the constants which are determined via the fitting of the experimental data at different C-rates ([Figure S1](#)). The capacity and discharge potential vs. Li, in a given voltage window, decrease when the discharge current increases. This trend can be quantified by the  $\alpha$  exponent in [Equation 1](#) as a lumped indicator: for every doubling in the current, the energy will drop by an approximate factor of  $\gamma = 0.301^\alpha$ , referred to as the rate-capability coefficient ( $0 < \gamma < 1$ ). Therefore, an electrode with a smaller  $\gamma$  suffers more from power limitations. Here, we report the  $\gamma$  values based on the discharge energy ([Table S2](#)).

### Electrochemical tests

Standard 2325 coin cells were assembled in an Argon-filled glove box. Electrodes were vacuum dried over night at 110°C before transferring to the glovebox. Lithium foil was used as the counter and reference electrode. The electrolyte was 1 M LiPF<sub>6</sub> in EC:EMC (3:7 w/w) and Celgard 2400 was used as the separator. All cells were tested using the Bio-Logic BSC-815 cycler. The cells were left at rest for 24 h before the formation cycles, i.e. three (dis)charge cycles at C/10. The upper and lower cutoff voltage limits were set to 4.3 V and 3.0 V, respectively. The rate capability of the electrodes was evaluated with a constant-current (CC) – constant voltage (CV) protocol composed of CC (dis)charge steps at C/10, C/5, C/2, 1C, 2C, and 5C. A CV step with the current limit of C/25 was in place to ensure a complete (de)lithiation.

### Particle size distribution (PSD)

The particle size distribution for the NMC622 powder was measured using a laser-based particle size counter setup (Malvern Mastersizer 2000; detection range between 0.05 and 1000 μm) and the results are summarized in [Figure. S2](#). A small amount of NMC powder was dispersed in Milli-Q water and the instrument laser was allowed to equilibrate for 1 h. Sample was added until an obscuration factor of 12.6% was attained. The measurement was carried out with a 2.4 mm beam length and a poly-disperse analysis model. The data are represented as volume distributions. 5 subsequent PSDs were recorded to check the stability of the dispersion, and the second measurement was reported.

### ALD coating

The NMC622 particles were coated using atomic layer deposition (ALD) in a rotating reactor by employing a titanium source (Tetrakis-dimethylamido-titanium (TDMAT)) and water as reactant ([Mattelaer et al., 2017](#)). After running one cycle of the process, theoretically a sub-monolayer of TiO<sub>2</sub> will be deposited on the surface of the particles. In the rotary ALD reactor, NMC particles are constantly tumbling to expedite exposure of the surface of the powder particles to the gaseous chemicals ([Longrie et al., 2012, 2014](#)). The reactor is first pumped down to a high vacuum (around 10<sup>-6</sup> mbar) and heated to 150°C. Then the TDMAT vapor enters the chamber. This gas stream connects to the reactor via a bubbler and is separated from the high vacuum chamber with an automatically controlled valve. The TDMAT reacts with the surface of NMC leaving behind a complex surface molecule containing Titanium. After a few seconds, the TDMAT valve is closed, and the residual gas left in the chamber is pumped away and the vacuum returns to base pressure. Once all the TDMAT gas has been evacuated from the chamber, a valve to the water bubbler is opened, allowing for water vapor to enter the reactor at a pressure of 5×10<sup>-3</sup> mbar to react with the complex Ti molecule on the NMC surface, resulting in TiO<sub>2</sub>. The thickness of the surface layer can be controlled by varying the number of cycles. This surface layer coating was 2 nm for this study.

The morphology and elemental analysis of the coated particles were investigated by a scanning electron microscope (FEI Quanta 200F) equipped with energy dispersive X-ray analysis (EDX). The SEM image and the corresponding EDX spectrum of the coated particles display the distinctive pick of Ti and conformal character of the coating, respectively ([Figure S5A and S5B](#)). XRF technique also confirms the presence of a vivid Ti peak ([Figure S5C](#)). In contrary to the high-magnification SEM with a focus on individual particles, in the XRF a higher number of particles are analyzed at once.

### Polarization analysis

Electrochemical techniques including rate capability tests, electrochemical impedance spectroscopy (EIS), cyclic voltammetry and pulse-relaxation methods have been broadly explored to give a deeper understanding of rate-limiting mechanism of the battery performance. Zheng et al. studied the impact of the cooperation between electrode components, electrode thickness and calendaring for the NMC111 cathode electrode in separate studies (Zheng et al., 2012a, 2012b). Morelly et al. showed the critical importance of short-range contact resistances as the rate limiting mechanism in NMC111 cathode based on a combination of rheological and rate capability tests (Morelly et al., 2018). However, their study was limited to two adjustable design parameters, i.e. porosity and thickness. Gao et al. employed galvanostatic intermittent titration technique (GITT) and EIS to study ultra-thick NMC electrodes (Gao et al., 2018a). They attributed capacity loss and under-utilization of active material to the poor effective Li diffusion in the porous electrode. Exploiting (semi)empirical relationships to describe the cell performance is another approach to study rate limitations (Gallagher et al., 2015; Heubner et al., 2019). Recently, in a sophisticated study, Tian et al. (Tian et al., 2019) studied more than 200 sets of experimental voltage versus capacity data extracted from the literature by setting up an empirical correlation between the rate performance and the electrode properties. Tomography-based techniques have been used successfully to correlate electrochemical performance, effective transport properties and 3D geometry of the electrode (Besnard et al., 2017). However, this approach is very tedious and cumbersome for investigating a large number of electrode designs. Physics-based macroscopic models offer an alternative approach compared to the empirical and semi-empirical methods for polarization investigations and optimization (Appiah et al., 2016). Malifarge et al. (Malifarge et al., 2018) used a physics-based modeling approach to study the impact of thickness and porosity on the polarization of high loading graphite anodes. They report that high-loading electrodes suffer less from particle-scale limitation compared to electrodes with low loading at any current density. Nyman et al. analyzed polarization in  $\text{LiNi}_{0.8}\text{Co}_{0.15}\text{Al}_{0.05}/\text{MAG10}$  electrodes based on the potential and concentration profiles (Nyman et al., 2010). They studied the sensitivity of the polarization regime to the charge/discharge conditions and battery designs. They concluded that all sub-processes have significant contributions to the cell polarization except for the ohmic losses in the solid phase.

In the present work, the so-called Newman battery model, based on the porous electrode and concentrated solution theories, was employed for a detailed polarization analysis of the sixteen NMC622 electrodes (Doyle et al., 1993). The 48 sets of experimental voltage-capacity plots from the 16 NMC622 electrodes discharged at three different C-rates (C/5, 1C, 5C) were compared against the simulation outputs. The only modification compared to the original model developed by Doyle et al. (Doyle et al., 1993) is the incorporation of multiple groups of active-material particles with different sizes (Figure S2) and contact resistances to the electronic and ionic percolation network of the electrode (Hamed et al., 2020). A summary of the model framework and its main parameters are shown in Tables S3 and S4, respectively.

The contribution of irreversible phenomena from the particle scale ( $\Omega_p$ ), short-range transport ( $\Omega_s$ ) and long-range transport ( $\Omega_l$ ) in the overall polarization of the NMC electrodes is determined by two main steps for each electrode design. First, the model adjustable parameters are determined to achieve the best match between the experiment and simulation for the three constant-current discharge profiles at C/5, 1C, and 5C. The parameters are optimized by a hybrid Genetic Algorithm (GA) and Nelder-Mead (NM) optimization technique to find the global minimum of the objective function. Second, the share of each physical/chemical phenomenon in the cell polarization is quantified by enabling or disabling its limiting role in the model. Here, disabling a physical phenomenon is referred to exclude its rate-limiting impact on the electrode performance via increasing its representative coefficient (e.g. rate constant) from the experimentally measured or optimally refined value to a relative infinity. The discharge-energy mismatch between the experiment and simulation is then compared for the two cases with enabled and disabled states to determine the polarization contribution. This procedure is exemplified in Figure S3 for the NMC622 electrode with an active-material loading of  $11.8 \text{ mg/cm}^2$  and porosity of 0.2.

The parameters in a physics-based model can be experimentally measured via different model-based approaches like those detailed in the literature and in our own previous works (Morelly et al., 2018). It is, however, important to realize that some parameters such as the electrode tortuosity or the effective lithium solid-state diffusion coefficient are very sensitive to the details of electrode preparation protocol. For instance, slight variations in the electrode processing can induce a large variation in the measured values for the parameters like diffusion and tortuosity which are very sensitive to the microstructural details

(Chouchane et al., 2020; Landesfeind et al., 2018; Kehrwald et al., 2011; Yari et al., 2020). This also partly explains why such parameters are usually scattered over a wide range in the existing literature (Amin and Chiang, 2016; Churikov et al., 2014; Chouchane et al., 2020; Pouraghajian et al., 2018; Usseglio-Viretta et al., 2018; Zahn et al., 2017). On the other hand, although a parameter like the exchange current density is rather feasible and easy to be measured, but more unconventional and complicated numerical and experimental procedures need to be followed for a parameter such as tortuosity (Ebner et al., 2014; Hutzenlaub et al., 2013; Malifarge et al., 2017; Thorat et al., 2009). This is reflected in the relatively small number of studies reporting the electrode tortuosity and also the large variance between the measured values depending on the techniques (tomography, EIS, etc.) and/or electrode preparation steps (Churikov et al., 2014; Usseglio-Viretta et al., 2018). In this regard, here, we follow a conservative approach for the parametrization of the solid-state diffusion coefficient and electrode tortuosity. We set the value of the solid-state diffusion coefficient to its lower limit and the electrode tortuosity to its upper limit. This approach will make our polarization analysis more representative of the usually observed particle agglomeration and micro-structural heterogeneity of the electrodes prepared in the labs.

Analyzing the surface and cross-sectional SEM images revealed that the size of the largest agglomerate in our NMC electrodes is about 23  $\mu\text{m}$  in diameter (Figure S4A). The lower limit for the solid-state diffusion coefficient was obtained by calculating an apparent diffusion coefficient assuming an equal time constant for the NMC particles with an average size of 12.7  $\mu\text{m}$  (Figure S2) and the agglomerate size (Figure S4A), i.e.  $\tau_{\text{diff}} = \frac{l^2}{D_1} \equiv \frac{l^2}{D_2}$ . This results in a value of  $\sim 4 \times 10^{-15} \text{ m}^2/\text{s}$  as the lower limit for the solid-state diffusion coefficient in contrast to the  $1.28 \times 10^{-14} \text{ m}^2/\text{s}$  which is the averaged measured diffusion coefficient in the NMC622 particles. It is worth mentioning that since only a portion of the active material in the electrode has undergone agglomeration, the calculation of the apparent diffusion coefficient, by considering all particles to be agglomerated, gives a conservative upper limit for the polarization induced by the lithium solid-state diffusion.

The upper limit for the tortuosity was set by using an upper limit for the Bruggman coefficient. According to the reported values for the effective transport properties for the spherical-active-material-based electrodes, a Bruggman coefficient of 2.5 can be considered as the upper limit of this value (Figure S4B). Moreover, we noticed that Bruggman coefficient values higher than 2.5 cause convergence problems in the numerical solution due to the severe ion depletion starting at very close position to the separator.

### Statistical analysis

The Pearson correlation coefficients corresponding to the data shown in the Figure 3 are listed in Table S5. The formula to calculate the Pearson correlation coefficient ( $r$ ) reads

$$r = \frac{\sum_i (x_i - \bar{x})(y_i - \bar{y})}{\sqrt{\sum_i (x_i - \bar{x})^2 \sum_i (y_i - \bar{y})^2}}$$

where  $x_i$  and  $y_i$  are the two variables under study and  $\bar{x}$  and  $\bar{y}$  are the average of  $x_i$  and  $y_i$ , respectively. A value of  $|r|$  close to 1 shows a strong correlation between the variables while a value of 0 bespeaks a weak correlation between the two variables.  $r > 0$  and  $r < 0$  indicates a direct and inverse proportionality, respectively, between  $x_i$  and  $y_i$ .

The Pearson coefficients corresponding to the diagonal subplots of Figure 3, highlighted in green in Table S5 are positive and higher than 0.5 for most of the operational conditions. This shows a relatively strong and direct correlation between the fractional change in the discharge energy ( $\Delta E$ ) and the related component of polarization.